Applied Catalysis B: Environmental 134–135 (2013) 174–184

Contents lists available at SciVerse ScienceDirect

Applied Catalysis B: Environmental

journal homepage: www.elsevier.com/locate/apcatb

Thorn-ball shaped TiO_2 nanostructures: Influence of Sn^{2+} doping on the morphology and enhanced visible light photocatalytic activity

Kishore Sridharan, Tae Joo Park*

Department of Materials Engineering, Hanyang University, Ansan 426-791, Republic of Korea

ARTICLE INFO

Article history:
Received 17 September 2012
Received in revised form 4 January 2013
Accepted 14 January 2013
Available online 23 January 2013

Keywords:
Thorn ball shaped nanostructures
Sn^{2+} doping
Titanium dioxide
Rutile
Hydrothermal
Photocatalysis
Visible light active
Photocatalyst
Rhodamine B
N de ethylation
Environmental remediation

ABSTRACT

A novel solution based route to synthesize thorn-ball shaped Sn^{2+} doped TiO_2 nanostructures in a large scale without the use of any reducing agents is demonstrated. White precipitates are formed instantaneously when a solution of cetyltrimethylammonium bromide with milli-molar quantities of stannous chloride dihydrate ($SnCl_2{\cdot}2H_2O$) is mixed to a solution of titanium isopropoxide in hydrochloric acid. The morphology of the precipitates analyzed using scanning electron microscope and transmission electron microscope reveal a complex morphology with crystalline nanorods grown uniformly over the balls. When the precipitates were treated hydrothermally by suspending in ethylene glycol (EG), further reduction takes place and "Thorn-ball shaped nanostructures" with very thin and long nanorods are formed. The thorn-ball samples (ST2-HTB) showed a large surface area of ~244 $m^2\,g^{-1}$ and the band-gap was ~0.3 eV narrower than that of pure TiO_2, P25 (~3.2 eV), enhancing its visible light absorption. The samples exhibited a superior efficiency in the photocatalytic degradation of Rhodamine B (RhB) under visible light irradiation to P25, and the efficiency was comparable to P25 under UV irradiation despite of their polycrystalline nature. Under visible light irradiation the degradation of RhB using thorn-ball nanostructure photocatalysts was accompanied by a gradual shift in the absorption peak owing to formation of several *N*-de-ethylated intermediates of RhB. Photodegradation reaction mechanism of RhB under visible light irradiation, was proposed to be initiated by the valence band holes or through the conduction band electrons. The novel strategy demonstrated here for preparing thorn-ball nanostructures opens a new horizon to design complex structures of TiO_2 for various applications.

1. Introduction

Solution based synthesis of nanostructures in a controlled fashion is a difficult yet important challenge with which the physical and chemical property of a material can be altered. A wide variety of synthetic techniques are available for controlling the size and dimensionality of a material of interest. In the past several years, semiconductor nanostructures have attracted significant research attention due to their size-tunable electronic and optical properties resulting in a wide range of applications in a number of scientific disciplines [1–6]. Semiconducting oxide nanostructures tend to exhibit unique properties such as large surface area, semi-directed charge transport and enhanced charge carrier mobility, which can be functionalized for applications in electronics and optoelectronics [7]. Among various semiconducting oxide nanostructures, titanium dioxide (TiO_2) has gained growing research interest as it is the most promising non-costly and environmental friendly wide band-gap semiconductor with applications in photovoltaics, photocatalysis, energy storage, sensing and so on [8]. It is well known that apart from crystal phase and particle size, the morphology (of TiO_2) also plays an important role in determining the device performance [9–11]. Solution based synthesis of TiO_2 nanostructures exhibiting diverse morphologies has been a major challenge owing to the rapid hydrolysis of titanium precursors [9]. Recently TiO_2 nanostructures with complex morphologies have been designed and developed hydrothermally by several research groups which tend to show exposed facets, large surface area and enhanced photoactivity [12–17].

Harvesting solar energy for environmental remediation and for solving the energy related issues relies on the development of visible light active photocatalysts. Improving the photocatalytic performance of TiO_2 nanoparticles under visible light irradiation has been a major research topic in the recent past [18]. It is well know that chemical doping of TiO_2 by the incorporation of additional metal or non-metal species can enhance the light absorption in the visible light region [18,19] and suppress the recombination of photogenerated charge carriers (electron–hole pairs) [20]. Photocatalytic activity of Sn^{4+} doped TiO_2 nanoparticles and thin

* Corresponding author.
E-mail address: tjp@hanyang.ac.kr (T.J. Park).

0926-3373/$ – see front matter © 2013 Elsevier B.V. All rights reserved.
http://dx.doi.org/10.1016/j.apcatb.2013.01.017

films have been studied under both UV (ultra violet) and visible light irradiations [20–25]. Boppanna and Lobo [26] reported the first experimental investigation on the visible light photocatalytic activity of Sn^{2+} doped with TiO_2. Oxides of Sn^{2+} have been well investigated owing to the presence of a lone pair cation, with the electronic configuration of $4d^{10}5s^25p^0$, is a suitable alternative to the oxides containing Pb^{2+} cations, and is environmentally safe. Hosogi et al. [27] studied the role of Sn^{2+} in the band structure of SnM_2O_6 and $Sn_2M_2O_7$ [M = Nb and Ta] along with the photocatalytic properties under visible light. Similarly the same group investigated the visible light photocatalytic properties of layered titanates and niobates by doping Sn^{2+} through ion-exchange [28]. Uma et al. [29] adopted the same ion-exchange synthesis methodology for the incorporation of Sn^{2+} ions in a few pyrochlore type oxide materials and investigated their visible light photocatalytic activity for studying the degradation of methyl orange dye. Li et al. [30] also adopted the same ion-exchange methodology to prepare Sn^{2+} doped potassium titanate nanoribbons and investigated the visible light hydrogen evolution and photodegradation of Rhodamine B dye. Su et al. [31] recently reported the hydrothermal preparation of $ZnWO_4$ nanocrystals doped with Sn^{2+} and its effect on the photodegradation of methyl orange dye under visible light. Reports so far suggest that Sn^{2+} doping reduces the band gap energy due to upward shift of the valance band resulting from the contribution of 5*s* band of Sn^{2+} to the O 2*p* band. Comparatively, band gap shifting or reduction is not seen in Sn^{4+} doped TiO_2 [32]. In this paper, we report for the first time a novel solution-based methodology for the synthesis Sn^{2+} doped TiO_2 nanostructures whose morphology represents a complex thorn-ball structure. White precipitates are formed when milli-molar quantities of $SnCl_2$ are added to TTIP solution. The precipitates grew into perfect thorn-balls when treated hydrothermally by mixing with EG. Influence of Sn^{2+} doping on the morphology was investigated using SEM and TEM. Photocatalytic degradation of Rhodamine B (RhB) dye is examined using the prepared thorn-ball nanostructures as photocatalysts. Results indicate that the samples are active photocatalysts with good efficiency under both UV and visible light irradiations. For an effective comparison, the photocatalytic activity of P25 TiO_2 (Degussa) was also investigated under the same experimental conditions.

2. Experimental procedure

2.1. Materials

Titanium tetraisopropoxide ($C_{12}H_{28}O_4Ti$, TTIP), hydrochloric acid (HCl, 20%) cetyltrimethylammonium bromide ($C_{19}H_{42}BrN$, CTAB), stannous chloride dihydrate ($SnCl_2{\cdot}2H_2O$) and ethylene glycol (EG) were purchased from Dae-Jung chemicals, Korea and were used as such without further purification. Deionized water was used throughout the experiments. For photocatalysis experiments, Rhodamine B (RhB) was purchased from Sigma–Aldrich (dye content ~ 95%). Commercial TiO_2 nanoparticles (P25) was purchased from Degussa.

2.2. Preparation of thorn-ball shaped TiO_2 nanostructures

Appropriate quantity of TTIP was dissolved in 15 ml of HCl (solution-A). An aqueous solution (solution-B) was prepared by dissolving 10 mM of CTAB and 5 mM of $SnCl_2{\cdot}2H_2O$ in 25 ml of DI water. Solutions A and B were mixed together under vigorous magnetic stirring to yield the precipitates (solution-C). Solution C was repeatedly centrifuged with DI water and ethanol for collecting the white precipitates. The pure precipitate was then dried in an oven at 100 °C for 10 h. The precipitate sample was named as ST-PTB (precipitate thorn-ball).

20 ml of solution-C was mixed with 30 ml of EG and this final solution was transferred to a 100 ml Teflon-lined stainless steel autoclave. The autoclave was sealed and the hydrothermal reaction was carried out at a temperature of 150 °C for 18 h. After the reaction was over, the autoclave was allowed to cool down naturally. The dark slurry containing white colored sediments was transferred to a clean beaker with the addition of excess ethanol. After the white sediments settled at the bottom, the dark colored solution was discarded. The white sediments were centrifuged several times with ethanol to remove impurities such as CTAB, HCl and EG. The pure sample obtained after centrifugation was dried in an oven at 100 °C for 10 h and was named as ST1-HTB (HTB – hydrothermally prepared thorn balls). Following the same procedure, samples ST2-HTB and ST3-HTB were prepared by increasing the $SnCl_2{\cdot}2H_2O$ concentration to 10 and 15 mM, respectively.

2.3. Preparation of 3D dendritic TiO_2 structures

TiO_2 structures were prepared following the same procedure as mentioned above, by eliminating the addition of $SnCl_2{\cdot}2H_2O$ in solution-B, which yielded a transparent solution-C. 20 ml of this transparent solution was mixed with 30 ml of EG and was treated hydrothermally under the same conditions followed previously 150 °C, 18 h. The slurry was centrifuged to obtain pure samples.

2.4. Characterization

The X-ray diffraction (XRD) patterns of the prepared samples were obtained using an X-ray diffractometer (*Rigaku-Dmax 2500*) with Cu-Kα radiation (λ = 0.15405 nm, 40 kV, 100 mA). The samples were scanned in the range 2θ = 20–80°. The morphology and energy dispersive X-ray spectroscopy studies (EDS) were performed using a *MIRA3 TESCAN* high resolution scanning electron microscope (SEM) equipped with a high brightness Schottky field emission gun. UV–vis diffuse reflectance spectrum (DRS) of the photocatalysts were recorded using *JASCO V-550* UV–vis spectrophotometer equipped with an integrating sphere (*JASCO ISV-469*) using a dedicated powder sample holder (*JASCO PSH-001*). The surface area and porosity of the samples were estimated by measuring the nitrogen adsorption–desorption isotherms on a *Micrometrics ASAP 2010* system. High-resolution transmission electron microscopy (HRTEM), EDS and selected area electron diffraction pattern (SAED) were performed on a *JEOL 2010F* FE-TEM operating at 200 kV. The samples for TEM were prepared by dropping a few drops of the sample solution dissolved in ethanol on a carbon-coated copper grid.

2.5. Photocatalytic studies

The photocatalytic activities of all the samples were assessed by observing the degradation of RhB under both UV and visible light irradiations. Reaction slurry was prepared in a crystallizing dish (*Duran®*) of 300 ml capacity by suspending 20 mg of photocatalyst in an aqueous solution of RhB (48.0 mg L^{-1}, 200 ml) which was stirred under dark for 1 h to ensure the adsorption of RhB on the surface of the photocatalyst. The experiments under UV light source were conducted under a UV lamp with the power of 300 W (Raynics, Korea). Visible light photocatalysis experiments were conducted in a home-made irradiation system, which was constructed using a 100 W halogen lamp (*HI-Spot 95*) purchased from *Osram Sylvania Inc.*, with UV-stop feature. The reaction slurry was placed on top of a magnetic stirrer, 6 cm below the source and was agitated at 200 rpm. For all samples, the UV and visible light photocatalysis experiments were carried out following the same procedure (as mentioned above) and aliquots were collected at regular intervals

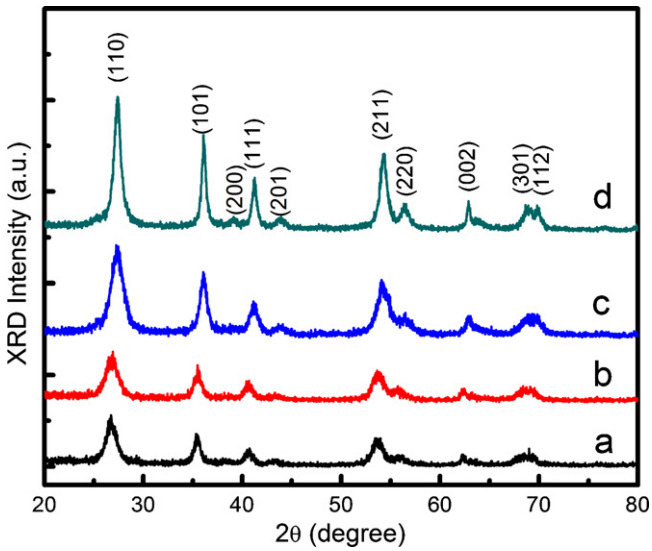

Fig. 1. XRD patterns of the as-synthesized samples. (a) ST3-HTB, (b) ST2-HTB, (c) ST1-HTB and (d) ST2-PTB.

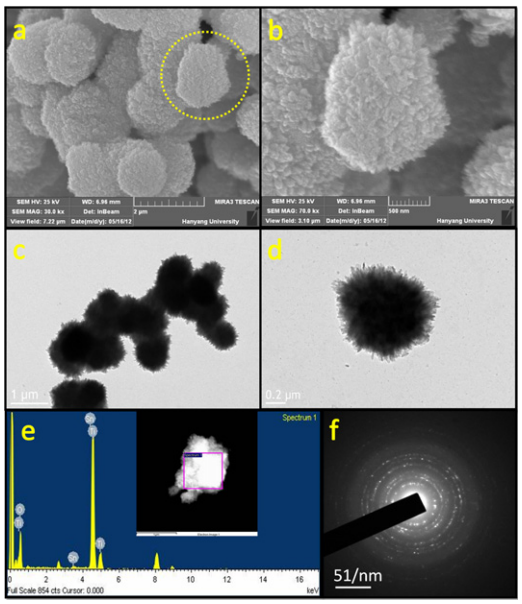

Fig. 2. (a and b) FE-SEM images of the Sn^{2+} doped TiO_2 precipitates. The encircled part in (a) is magnified in (b). (c) Large area, (d) single particle TEM image of the precipitates revealing the presence of short thorns. (e) EDS spectra from the square area marked on the image in the inset and (f) SAED pattern from the area of the thorn-ball as shown in (d).

of time for both the cases. UV–vis absorption spectra of the aliquots were recorded on a *JASCO V-550*, UV–vis spectrophotometer.

3. Results and discussion

The XRD patterns of the as-synthesized products are shown in Fig. 1. All the observed peaks in the ST samples including the precipitates can be indexed to the pure tetragonal rutile phase of TiO_2 (JCPDS card # 21-1276) with lattice constants $a = 4.593$ Å and $c = 2.985$ Å.

3.1. Growth of thorn-ball precipitates

The main factor governing the growth of thorn-ball nanostructures (ST-PTB) through solution-based synthesis route is the controlled hydrolysis of titanium precursor [9,33,34]. The dissolution of TTIP in excess of HCl, significantly lowers the pH of the solution, and thus slows down the hydrolysis of TTIP. Formation of a white precipitate (Fig. S1a, Supplementary content) is noted when DI water solution containing CTAB and $SnCl_2{\cdot}2H_2O$ (solution B) is added to the TTIP in HCl solution (solution A) under vigorous stirring. When left for several hours without stirring the precipitates settle down at the bottom of the beaker indicating the formation of particles after nucleation. $SnCl_2$ dissolved in HCl acts as a strong reducing agent [35] which is believed to be the reason for the formation of white precipitate. Fig. 2a and b shows the FE-SEM image of as-synthesized precipitates (ST2-PTB) and the magnified view of the precipitates captured from the area indicated in Fig. 2a, respectively. As seen from Fig. 2b, rough spiny surface is formed all over the precipitates due to the action of HCl, which probably could etch the surface of the TiO_2 when the solution is aged before being washed. The large area TEM image in Fig. 2c, clearly reveals that the surface of the precipitates are etched uniformly, forming short thorns which is finally patterned as like a thorn-ball structure, as seen in Fig. 2d. The EDS spectra of the precipitates were obtained by scanning over the square area marked on the bright field TEM image shown in the inset of Fig. 2e. The amount of Ti, O and Sn were 80.2, 18.5 and 1.3 wt% (58.89, 40.72 and 0.39 at%) respectively. The SAED pattern shown in Fig. 2f were obtained from the area as seen in Fig. 2d, the ring diffraction pattern suggests the polycrystalline nature of the precipitate thorn-ball (ST2-PTB).

Fig. 3a and c are the magnified TEM images of the top and bottom area of the precipitate ST2-PTB (as seen in Fig. 2d), depicting a uniform growth of nanorods over the balls, with an average diameter of ~25 nm. The HRTEM images shown in Fig. 3b and d were captured from the rectangular areas marked in Fig. 3a and c, respectively, clearly reveals the crystalline nature of the nanorods. The lattice resolved HRTEM images shown in the insets of Fig. 3b and d were obtained from different regional parts of the nanorods (encircled area), illustrate the nearly parallel atomic planes with two different d-spacing values of 3.25 and 2.49 Å representing the {1 1 0} and {1 0 1} crystal planes of rutile TiO_2, respectively. The HRTEM analysis on the other areas of the precipitates revealed the dominant presence of {1 1 0} plane of rutile TiO_2, is consistent with the XRD results.

3.2. Growth of thorn-ball nanostructures under hydrothermal conditions

In a study on the hydrothermal preparation of 1D titanium glycolates [36] EG was employed as a solvent as well as reducing agent. The authors found out that, EG not only reduced the rate of hydrolysis but also assisted the assembly of titanium atoms into 1D form. Similarly in another study on the growth of lutetium oxide [37], EG played a similar role under hydrothermal conditions, wherein a metastable supersaturated solution was formed and the precursors underwent homogeneous nucleation to form a 3D flower-like morphology. The growth of the present thorn-ball shaped nanostructures (ST-HTB) prepared hydrothermally can be speculated to follow these two steps: (1) The precipitate solution (pH ~ 0) added to EG under hydrothermal conditions, undergoes further reduction in the presence of $SnCl_2$ as a reducing agent, and (2) EG acts as a co-solvent/co-surfactant and plays a vital role in the assembly of nanorods over the top of the nucleated spheres.

The morphology of the hydrothermally synthesized samples (ST2-HTB) observed using FE-SEM and TEM are shown in Fig. 4a–d,

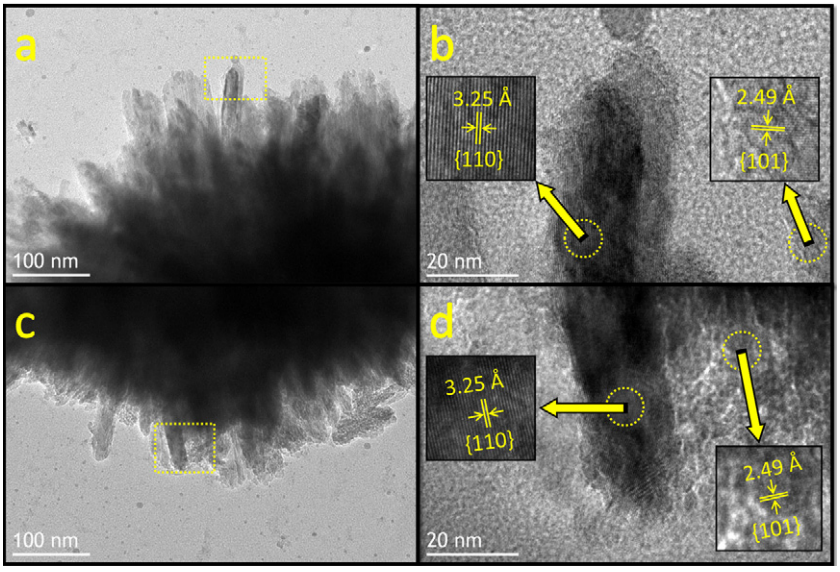

Fig. 3. (a and c) TEM images showing the top and bottom area of Fig. 2d. (b and d) HRTEM images from the rectangular area indicated in (a) and (c) and the lattice resolved images of different regional parts are shown in their insets.

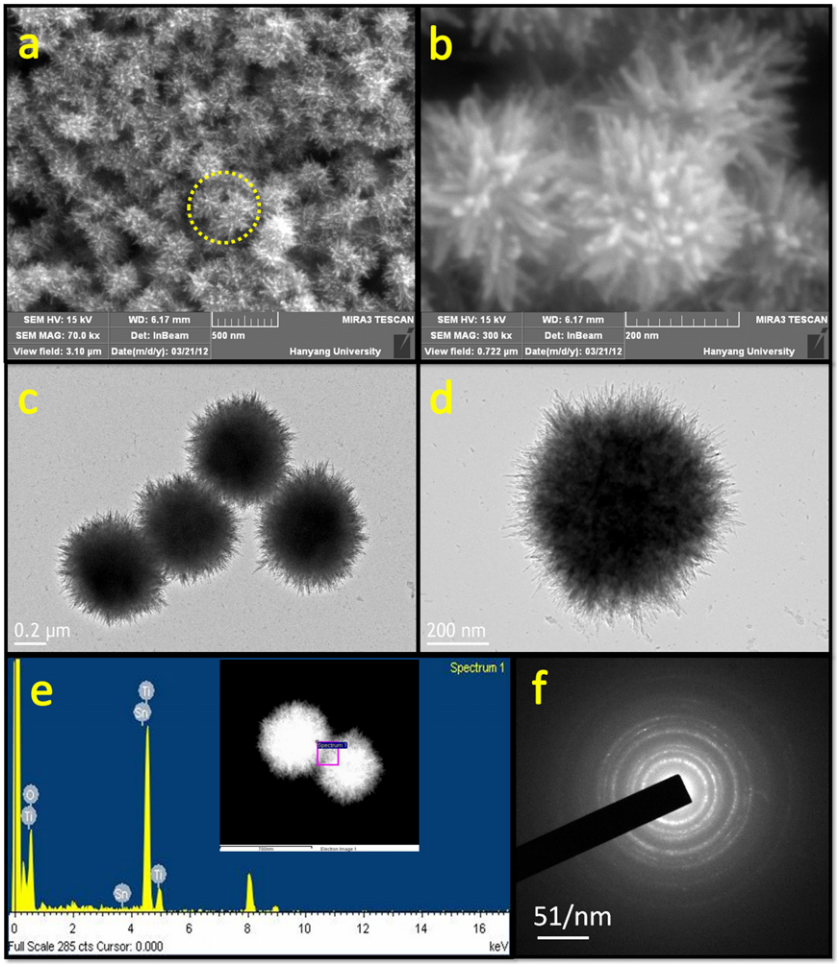

Fig. 4. (a and b) FE-SEM and (c and d) TEM images of the thorn-ball like Sn^{2+} doped TiO_2 nanostructures, respectively. The encircled part in (a) is magnified in (b). (e) EDS spectra from the square area marked on the image shown in the inset and (f) SAED pattern of the thorn-ball shown in (d).

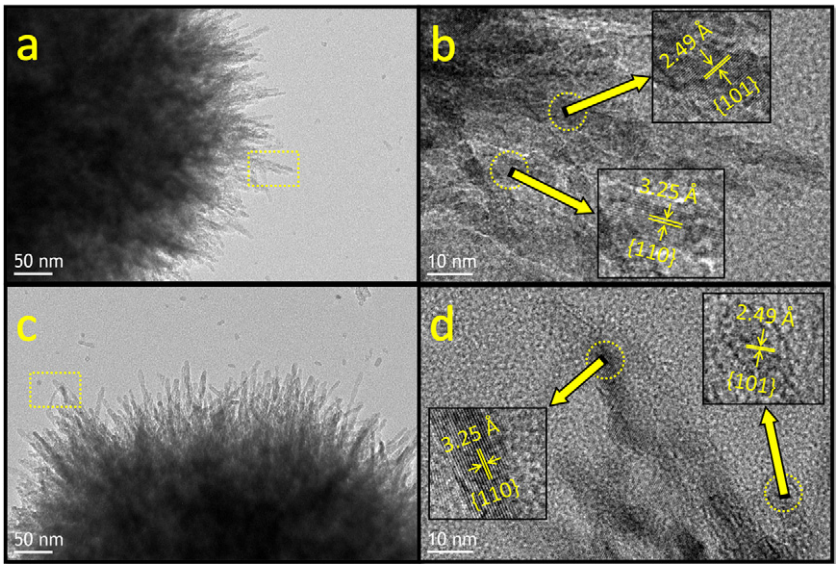

Fig. 5. (a and c) TEM images showing the right side and top area of Fig. 4d. (b and d) HRTEM images of the rectangular area marked in (a) and (c) and the lattice resolved images of different regions are shown in the inset.

respectively. The morphology of the structures as seen in Fig. 4b–d, clearly mimic a thorn-ball like structure. The EDS spectrum shown in Fig. 4e was obtained by scanning over the square area marked on the bright field TEM image shown in its inset. The EDS spectrum showed no impurities and the amount of Ti, O and Sn were 72.5, 26.9, and 0.5 wt% (47.25, 52.62 and 0.13 at%) respectively. Fig. 4f represents the SAED ring type pattern acquired from a single thorn-ball (Fig. 4d) which shows the polycrystalline nature of the hydrothermally prepared samples. The FE-SEM images of the samples ST1-HTB and ST3-HTB under different magnifications are given in the Supplementary content, Figs. S2 and S3, respectively. The EDS spectrum, quantification data and elemental maps studied using FE-SEM on the samples ST1-HTB, ST2-HTB and ST3-HTB are given in Supplementary content, Fig. S4.

The TEM images in Fig. 5a and c are the magnified view of the right side and top part of the thorn-ball nanostructure (as seen in Fig. 4d), respectively. Though the nanorods are uniformly arranged, they are randomly oriented with respect to each other and thus their growth directions are unique. The average length and diameter of the nanorods (thorns) are found to be ~50 nm and ~10 nm respectively, is significantly smaller in comparison to the average diameter of the nanorods formed on the precipitates, owing to the heavy etching of the surface by HCl during hydrothermal preparation. The HRTEM images shown in Fig. 5b and d are captured from the rectangular area marked in Fig. 5a and c, respectively. The lattice resolved HRTEM images obtained from different regional parts (encircled areas) are shown in the insets of Fig. 5b and d. The spacing in between two adjacent planes was found to be 3.25 and 2.49 Å corresponds to the {1 1 0} and {1 0 1} planes of rutile TiO_2, respectively. Though the size of the nanorods formed on the precipitates varied under hydrothermal conditions, the {1 1 0} plane was still found to be the dominant and is consistent with the XRD results.

When $SnCl_2{\cdot}2H_2O$ was not added to solution-B, a transparent solution-C is formed (Fig. S1b in Supplementary content). Hydrothermal reaction by the addition of EG with this solution-C, resulted in the formation of 3D dentritic TiO_2 structures. The FE-SEM images shown in Fig. 6 represent these 3D TiO_2 structures. These samples are bigger in size than those of the precipitates (ST-PTB) and the hydrothermally formed Sn^{2+} doped TiO_2 thorn-ball structures (ST-HTBs). Thus, it is very clear that the addition of $SnCl_2{\cdot}2H_2O$ significantly modifies the particle size and shape from 3D dendritic to thorn-ball like structures.

3.3. Surface area and energy band-gap measurements

The catalytic efficiency of a photocatalyst is dependent on its surface area and crystallinity [38]. The BET surface area of ST2-HTB was 244 $m^2\,g^{-1}$ and ST1-HTB was 236 $m^2\,g^{-1}$ which is 4.5 times more than that of the surface area of pure P25 nanoparticles (50 $m^2\,g^{-1}$) [38] (nitrogen adsorption–desorption isotherms are shown in Supplementary content, Fig. S5). The surface area of ST3-HTB should obviously be larger than those of ST1-HTB and ST2-HTB considering that the particle size of ST3-HTB (~200 nm) is smaller than those of ST1-HTB and ST2-HTB (~350 and ~250 nm as shown in Fig. S2 and Fig. 4, respectively). The energy band-gap from the UV–vis DRS spectra were calculated using the Kubelka–Munk theory. The Kubelka–Munk function for reflectance, $F(R)$ is given as,

$$F(R) = \frac{(1-R)^2}{2R}$$

where reflectance $R = R_{sample}/R_{reference}$. Tauc plots are constructed using the Kubelka–Munk [39,40] function for reflectance, $[F(R)\cdot h\nu]^{1/2}$ versus $h\nu$ and the indirect band gap energies were deduced by extrapolating the linear portion of Tauc's equation onto the energy axis as shown in Fig. 7b. The estimated energy band gap of P25 TiO_2 is ~3.2 eV and for ST-HTB and ST-PTB samples it was estimated to be ~2.95 eV.

Density functional theory (DFT) calculations on Sn^{2+} doped TiO_2 predict that the band gap shifting can be dependent on either the location of the substitutional Sn cation [41] or due to the lowering of the conduction band energy [42]. Sn^{2+} lone pair cations are more easy to be accommodated on the surface sites, rather than in the bulk, provide driving force for surface segregation [43,44]. Unoccupied presence of Sn^{2+} lone pair on the surface of a perfect crystal would lead to the rearrangement of the nearest neighbors giving rise to lattice deformation [45]. Band gap shifting can thus take place due to the small binding energy of the electronic levels introduced by the surface doped Sn^{2+} ions, that are located close to the valence band [46]. Su et al. [31] recently reported a linear relationship between shift in the band gap energy with respect to the lattice volume or particle size for Sn^{2+} doped $ZnWO_4$ nanocrystals and predicts this to be used for optimizing the photocatalytic degradation efficiency. Thus the above discussed mechanism for the presence of Sn^{2+} lone pair of electrons is responsible for the

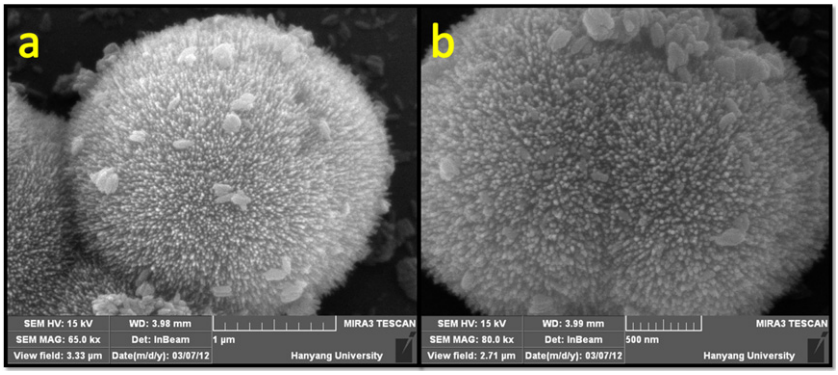

Fig. 6. FE-SEM images of 3D TiO_2 structures in two different magnifications.

shift in the energy band gap in case of our thorn-ball (ST-HTB and ST-PTB) samples.

3.4. Photocatalytic degradation of RhB and its reaction mechanism

When light is irradiated on a system containing the dye molecules that are adsorbed on top of a semiconductor (reaction slurry), electron–hole pairs are created and the average transit time (τ) for carrying the randomly generated charge carriers from the bulk to the surface is given by the relation $\tau = r^2/\Pi^2 D$, where r is the grain radius and D is the coefficient of diffusion [47]. Smaller the grain size, larger is the charge transfer ability from the bulk to the surface [48]. Therefore, larger surface area and effective charge transport can enhance the photocatalytic degradation of RhB dye.

3.4.1. UV light photocatalysis

UV–vis absorption spectra in Fig. 8 show the photocatalytic degradation of RhB under UV light irradiation in the presence of ST2-HTB, ST3-HTB, ST2-PTB and P25, and have been summarized with respect to irradiation time as in Fig. 8e. Under UV light irradiation, P25 (pristine TiO_2) nanoparticle sample exhibited a better efficiency in the degradation of RhB in comparison to thorn-ball samples. This can be attributed to its small particle size (~25 nm), and its dominant anatase phase (>80%) of TiO_2 with highly photoactive {0 0 1} facets [48–50]. The photocatalytic degradation efficiency of Sn^{2+} doped TiO_2 thorn-ball samples (ST-HTB) are comparatively lesser than P25 due to their polycrystalline nature. Despite its polycrystalline nature the degradation efficiency of ST3-HTB is comparable to P25 owing to its large surface area with several thorny nanorods of diameter ~ 10 nm. The overall photocatalytic activity of hydrothermally prepared thorn-ball (ST-HTB) samples (Fig. 8a and b) can be attributed to its complex morphology surrounded by randomly oriented nanorods with dominant {1 1 0} rutile facets [51], which are photoactive. It is also possible that, when UV light is irradiated, multiple reflections can take place over the sharp thorns (Fig. 4c), thereby enhancing the number of photogenerated electrons and holes to take part in the degradation of RhB [52,53]. Sn^{2+} doped TiO_2 precipitate (ST2-PTB) thorn-ball sample showed the least degradation efficiency (Fig. 8c), could be due to its polycrystalline nature and small surface area (particle size of ~1 μm, as seen in Fig. 2b), which reduces the charge transfer ability from bulk to the surface. Compared to the hydrothermally prepared thorn-balls, the surface of the precipitates is surrounded by short nanorods with blunt edges (Fig. 3a), may scatter the light irradiated on its surface. Moreover, the scattering of the incoming light due to presence of large size particles [54] could be speculated as a reason for the reduced efficiency of degradation. The photocatalytic reaction mechanism for the degradation of dyes using TiO_2 under UV light has been well documented in literature [55–57]. In brief, UV light ($\lambda < 387$ nm) irradiation on TiO_2 induces adsorption of photons which in turn excites an electron (e_{CB}^-) to the conduction band (VB) creating a positive hole (h_{VB}^+) in the valence band (VB). The positive holes oxidize water to produce $OH^\bullet$ radicals that can oxidize organic species present. Molecular oxygen adsorbed on the surface of TiO_2 trap the electrons in CB and get reduced as superoxide radical anion $O_2^{-\bullet}$ which react further with H^+ and generates hydrogen peroxide radical $^\bullet OOH$. Electron–hole pair recombination is a major limitation in semiconductor photocatalysis, but in P25 TiO_2, the rutile phase (~20%) acts as an electron sink reduces the recombination [58]. Along with reduced recombination rate, P25 TiO_2 nanoparticles has a band gap of ~3.2 eV which is capable of efficiently trapping UV light and thus show enhanced photocatalytic efficiency in the degradation of RhB in comparison to thorn-ball nanostructures.

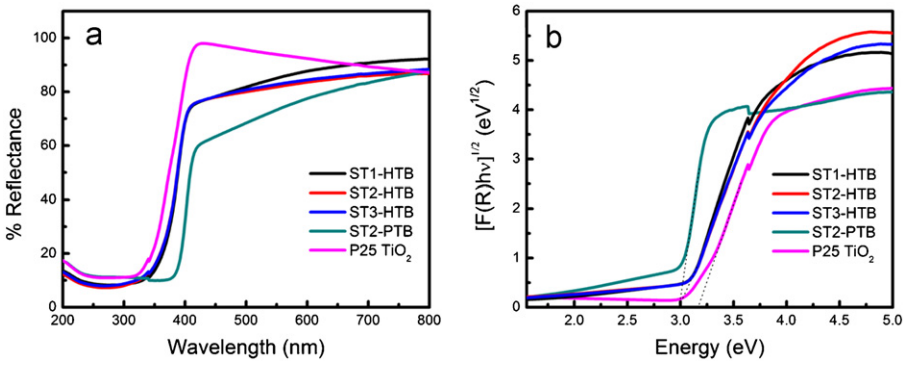

Fig. 7. UV–vis diffused reflectance spectra (a) of the photocatalysts and their corresponding Tauc's plots (b).

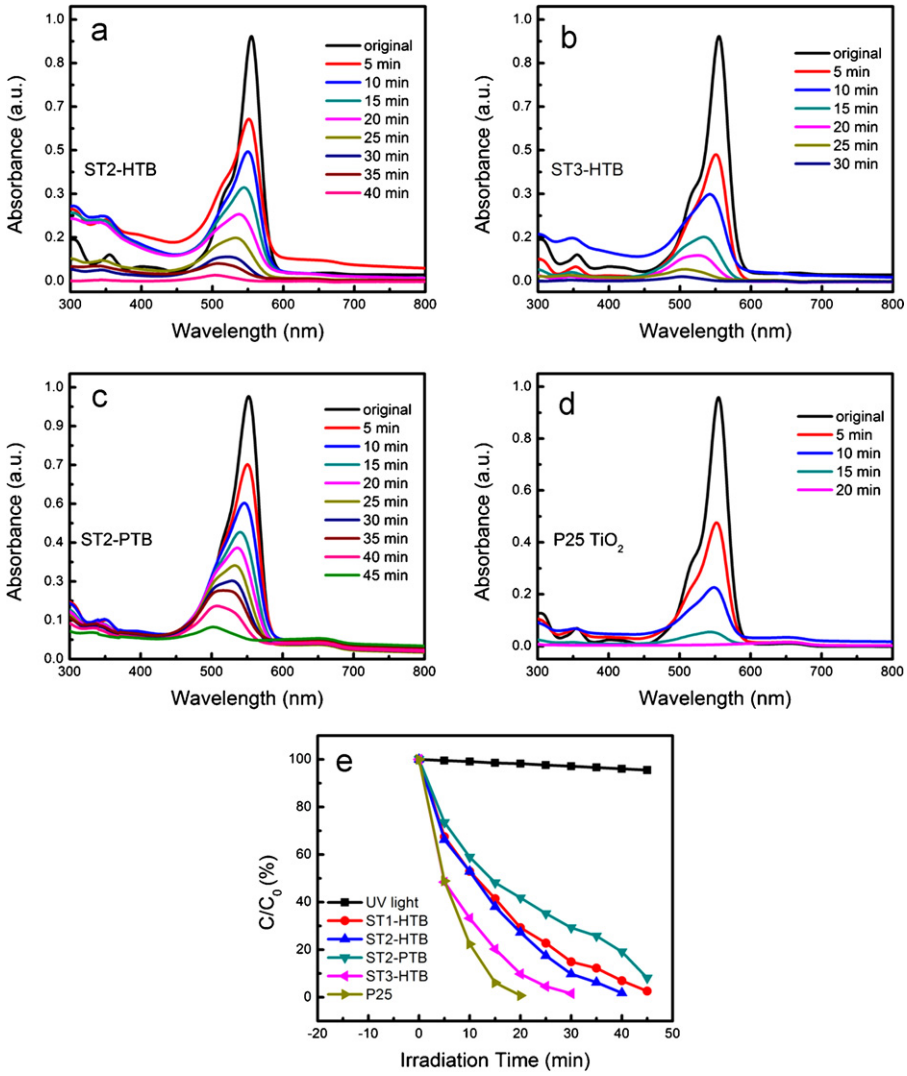

Fig. 8. UV–vis absorption spectra showing the gradual degradation of RhB under UV light irradiation in the presence of (a) ST2-HTB, (b) ST3-HTB, (c) ST2-PTB, (d) P25, and (e) UV light assisted photocatalytic degradation of RhB with respect to irradiation time.

3.4.2. Visible light photocatalysis

In visible light photocatalysis experiments ($\lambda \geq 400$ nm), the hydrothermally prepared Sn^{2+} doped TiO_2 thorn-ball (ST2-HTB and ST3-HTB) samples exhibited better photocatalytic activity than ST2-PTB and P25 as shown in Fig. 9. The larger surface area and narrower band-gap of sample ST2-HTB and ST3-HTB enhances the photocatalytic degradation efficiency in comparison to P25. Sample ST2-PTB showed poor efficiency in the degradation of RhB under visible light, due to the same reasons as in UV-light assisted photocatalysis. When visible light is illuminated, the RhB dye molecules adsorbed on the surface of P25 TiO_2 nanoparticles get excited and inject electrons (e^-) into the conduction band (CB) of TiO_2. The injected electrons are scavenged by molecular oxygen to form superoxide radical $O_2{}^{-\bullet}$ and hydrogen peroxide radical $^{\bullet}OOH$ [59]. These radicals help in decolorizing RhB by destroying their chromophore structure. It should be noted that, only under UV light assisted photocatalysis of TiO_2 an e–h pair is generated in TiO_2. Visible light photocatalysis in TiO_2 takes place through dye sensitization and no holes can be formed in the valence band of TiO_2 corresponding to the injected electrons in the CB [60].

It was interesting to observe that the absorbance peak intensity of RhB dye centered at ~554 nm (λ_{max}) gradually decreased until a certain time after which the peak gradually shifted toward the blue end of the spectrum with a final central maximum of (λ_{max}) ~496 nm for all the samples except for P25 as shown in Fig. 9a–c. The stepwise removal of ethyl group ($-C_2H_5$) attached to the nitrogen atom in Rhodamine B molecule, during its photocatalytic degradation is termed as *N*-de-ethylation process. Scheme 1 shows a schematic of the *N*-de-ethylation process that could undergo in Rhodamine B. The absorbance peak shifting phenomenon was found to occur only under visible light irradiation and can be compared with the absorption spectra shown in Fig. 8a–c (UV light assisted RhB degradation). The change in the absorbance peak position (λ_{max}) was in direct correlation with the change in the color of the aliquots collected at regular intervals of time. The gradual color of the dye containing the photocatalyst at different time intervals is shown in Fig. 10a. *N*-de-ethylation in P25 TiO_2 nanoparticles is reported to happen very slowly [59] and since we irradiated visible light only for a period of 100 min, we hardly observed a significant peak shifting due to *N*-de-ethylation. In detail, during the degradation of RhB using ST2-HTB photocatalyst under visible light irradiation (Fig. 9a), the main absorbance peak of RhB (at ~554 nm) shifted gradually to $\lambda_{max} \sim 500$ nm (obvious from the color change to light green as seen in Fig. 10a) after 60 min of irradiation, and did not change any more but the peak intensity decreased further. After 90 min of irradiation, ~90% of the RhB dye degraded and the

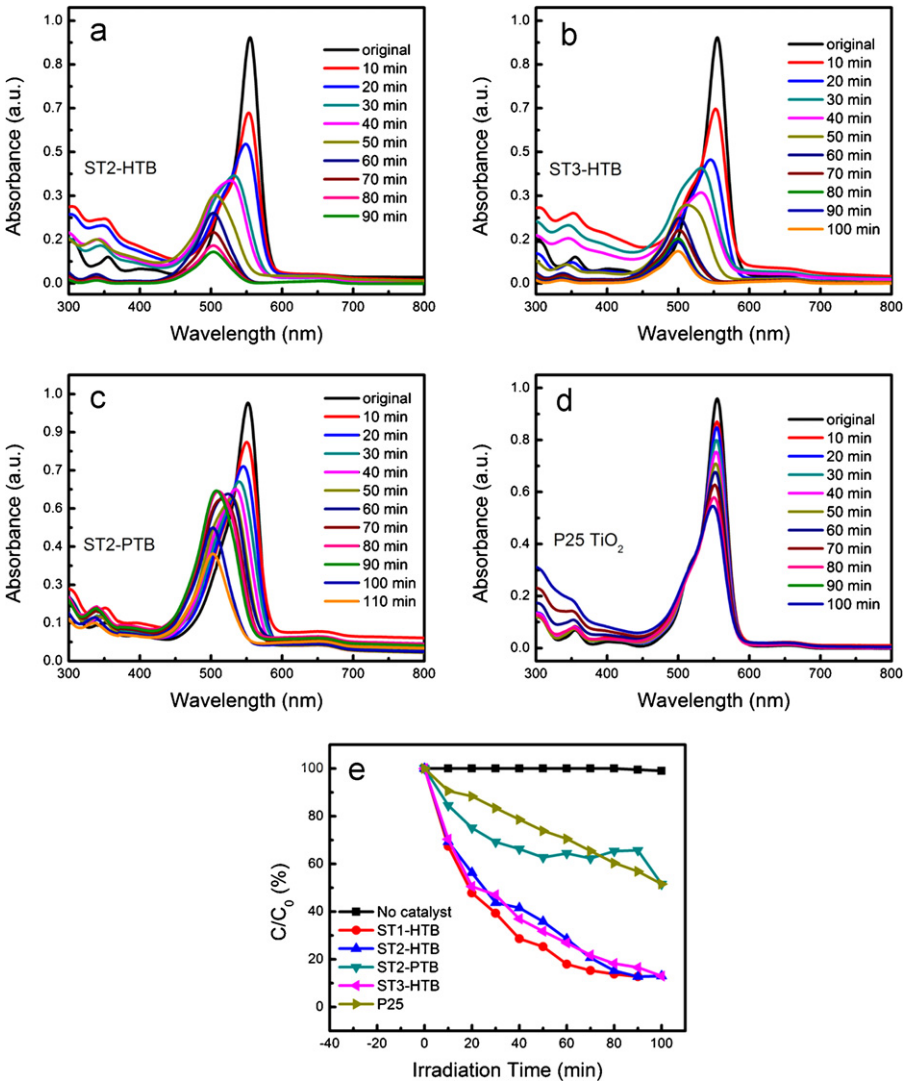

Fig. 9. UV–vis absorption spectra showing the gradual degradation of RhB in the presence of (a) ST2-HTB, (b) ST3-HTB, (c) ST2-PTB, (d) P25 samples as photocatalysts under visible light irradiation, and (e) visible light assisted photocatalytic degradation of RhB with respect to irradiation time.

color of the aliquot almost looked transparent (Fig. 10a). Similar peak shifting was observed in sample ST3-HTB and 90% of RhB dye degraded after being irradiated for 100 min. The gradual shift in the absorption peaks toward the blue region of the spectrum in case of ST2-PTB is shown in Fig. 9c. After 110 min of irradiation, ~60% of RhB dye degraded. *N*-de-ethylation was previously observed by several groups while they studied the photocatalytic degradation of RhB under visible light [26,30,59,61]. Their studies predict the formation of several partially *N*-de-ethylated intermediates with different absorbance peaks (λ_{max}). The peak observed at ~500 nm, formed during the degradation of RhB was predicted to be the final de-ethylated product called Rhodamine (Rh) [30]. Fig. 10b shows the picture of the aliquots collected from the UV light assisted degradation of RhB in the presence of ST2-HTB as the photocatalyst. This suggests that the absorbance peak shifting by the formation of *N*-de-ethylated intermediates was quite suppressed under UV light irradiation which could be due to the high intensity of UV light irradiation (300 W) and a faster rate of RhB degradation.

Visible light absorption is induced in Sn^{2+} doped TiO_2 thorn-balls samples owing to the shift in the band gap due to the presence of Sn^{2+} ions on the surface sites. Boppana et al. [26] used the fluorescence technique [62] for confirming the formation of hydroxyl radicals and found a linear increase in the fluorescence intensity by using 2-hydroxy terephthalic acid. Photocatalytic degradation of RhB was proposed via indirect oxidation by hydroxyl radicals $OH^{\bullet}$. Mechanism of *N*-de-ethylation on TiO_2 materials [63] is mechanized as a surface process with enhanced adsorption of the dye on the catalyst surface. Sn^{2+} doped TiO_2 prepared by Boppana et al. had a large surface area and the *N*-de-ethylation decomposition profile of RhB were analyzed using chemometric tools [26]. The ST-HTB thorn-ball samples prepared by us also have a large surface area of ~244 $m^2\,g^{-1}$, with greater chances of enhanced dye adsorption on the surface of the catalyst. Moreover, the unique thorn-ball shape can offer more reaction sites. We analyzed the *N*-de-ethylated intermediates from the UV–vis spectra shown in Fig. 9. The *N*-de-ethylated species formed in between 554 nm and 498 nm are consistent with the reports in literature [26,30,59,61].

In case of Sn^{2+} doped TiO_2 thorn-ball structure, the reaction mechanism could possibly follow two pathways, viz. photodegradation initiated by valence band holes via indirect oxidation by hydroxyl radicals (path I) and photodegradation initiated by conduction band electrons (path II). Though pathway I has been the most prominent for the RhB degradation using Sn^{2+} doped TiO_2 [26], yet the possibility of pathway II cannot be ruled out. Schematic

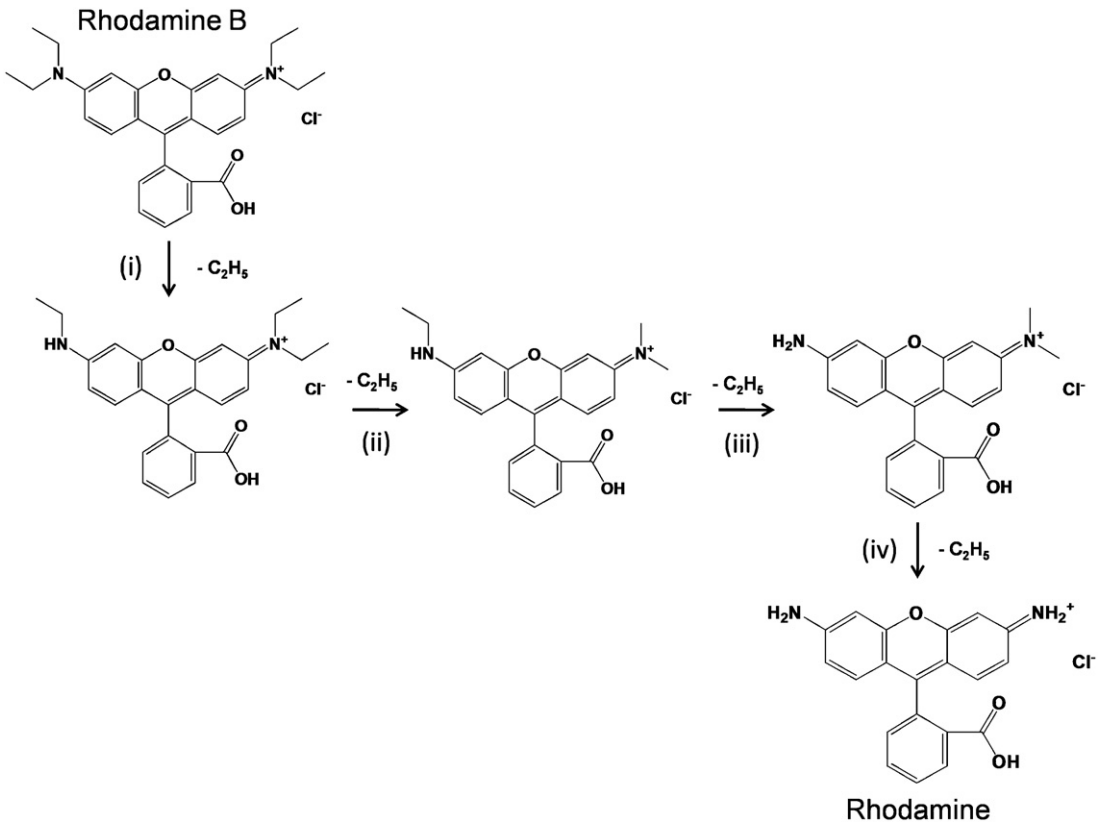

Scheme 1. Proposed reaction pathways for *N*-de-ethylation of RhB under visible light induced photocatalysis.

2 illustrates the photodegradation of RhB using Sn^{2+} doped TiO_2 (ST-HTB) thorn-ball samples.

As per path I, photogenerated holes are created when visible light is irradiated on the surface of the thorn-ball (ST-HTB) photocatalyst. RhB molecules adsorbed on the thorn-ball surface trap these photogenerated holes and get converted to cationic radicals (RhB^+) [19,61]. *N*-de-ethylation is then continued as has been discussed in path I. The reaction steps could be given as follows:

$$\text{ST-HTB} \rightarrow h^+_{VB} + e^-_{CB}$$

$$RhB_{ad} + \text{ST-HTB}(h^+_{VB}) \rightarrow RhB^+ + \text{ST-HTB}$$

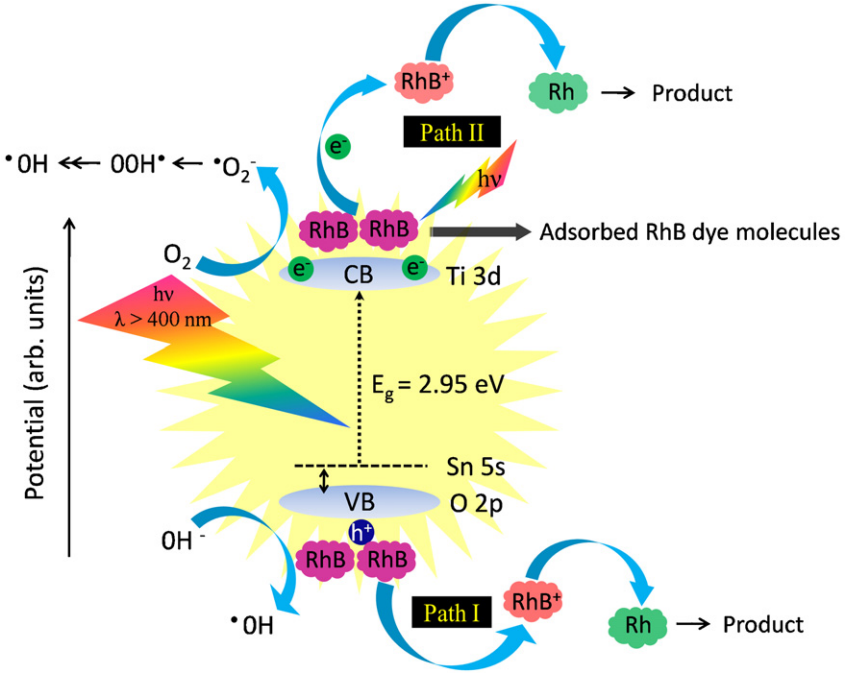

Scheme 2. Photocatalytic reaction mechanism of RhB degradation using thorn-ball nanostructures under visible light irradiation.

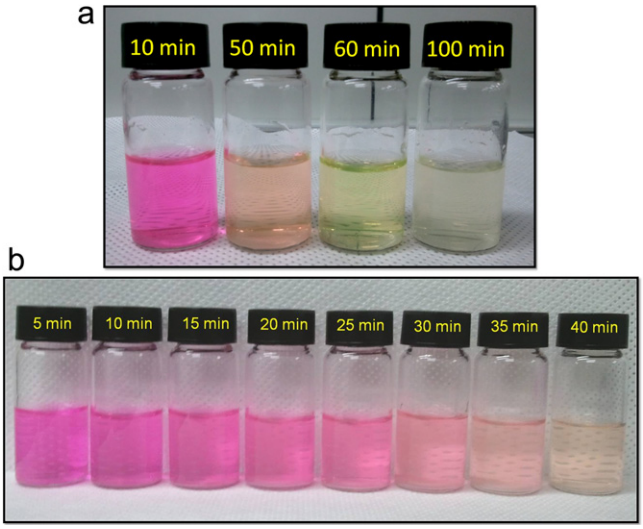

Fig. 10. (a) Aliquots indicating the color change at 10, 50, 60 and 100 min during the degradation of RhB in the presence of ST2-HTB under visible light irradiation, and (b) aliquots collected at regular intervals of time (5 min) during the degradation of RhB in the presence of ST2-HTB as the photocatalyst under UV light irradiation. (For interpretation of the references to color in the text, the reader is referred to the web version of this article.)

$$RhB^{+}_{ad} \xrightarrow{N\text{-de-ethylation}} \text{Rhodamine} \rightarrow \text{intermediates} \rightarrow \text{degraded products}$$

According to path II, the RhB molecules adsorbed on the surface of the ST-HTB (RhB_{ad}) samples are excited by visible light irradiation, which injects an electron into the conduction band of ST-HTB sample. Cationic radical, RhB^{+} formed during the previous step is scavenged by the molecular oxygen to form superoxide $O_2^{-\bullet}$ and hydrogen peroxide radical $^{\bullet}OOH$. Chromophore of RhB is thus destroyed and the dye is *N*-de-ethylated to Rhodamine (Rh). Photooxidation continues to go on and thus intermediates and degraded products are obtained [55,61]. The reaction steps involved are given below:

$$RhB_{ad} + h\nu \rightarrow RhB^{*}_{ad}$$

$$RhB^{*}_{ad} + \text{ST-HTB} \rightarrow RhB^{+}_{ad} + \text{ST-HTB}(e^{-})$$

$$\text{ST-HTB}(e^{-}) + O_2 \rightarrow \text{ST-HTB} + {}^{\bullet}O_2^{-} \rightarrow\rightarrow {}^{\bullet}OOH \text{ and } {}^{\bullet}OH$$

$$RhB^{+}_{ad} \xrightarrow{N\text{-de-ethylation}} \text{Rhodamine} \rightarrow \text{intermediates} \rightarrow \text{degraded products}$$

Despite the polycrystalline nature, all hydrothermally prepared Sn^{2+} doped TiO_2 (ST-HTB) thorn-ball samples exhibited good photocatalytic efficiency in the degradation of RhB dye under visible light irradiation due to their large surface area with thorny nanorods and the narrower band-gap. It is worth noting that the photocatalytic degradation of RhB using the as-synthesized photocatalyst were carried out using a halogen lamp with a low power of 100 W with the concentration of RhB being 48 mg L^{-1}. Moreover, only 20 mg of the photocatalyst sample was added to 200 ml of aqueous solution of RhB, and by this we believe that the prepared samples have shown good efficiency in the degradation of RhB.

4. Conclusion

We demonstrated the preparation of Sn^{2+} doped TiO_2 thorn-ball nanostructures with high photocatalytic efficiency. White precipitates with a complex structure was formed instantaneously when $SnCl_2{\cdot}2H_2O$ was added to a solution containing TTIP in HCl. Controlling the rate of hydrolysis of TTIP and the addition of $SnCl_2{\cdot}2H_2O$ were critical in the formation of initial thorn-ball structures in the form of precipitates. Hydrothermal reaction in the presence of EG led to the formation of the final thorn-ball nanostructures. The surface area of all the thorn-ball samples was significantly high and incorporation of Sn^{2+} in TiO_2 reduces its band-gap enhancing visible light absorption. The photocatalytic efficiency of the samples was comparable to P25 under UV irradiation and exhibited a better efficiency under visible light irradiation despite of the polycrystalline nature. The complex thorn-ball morphology allows multiple reflection of the irradiated light over its surface, thereby enhancing the rate of degradation. Under visible light irradiation, Rhodamine B degraded in steps forming several *N*-de-ethylated intermediates which were confirmed from the changes in the absorbance peak and the color of the dye solution. In addition to photocatalytic degradation of RhB due to indirect oxidation by hydroxyl radicals, dye sensitized photodegradation could also happen. The thorn-ball nanostructures of Sn^{2+} doped TiO_2 could possibly find applications in dye-sensitized solar cells, fuel cells and as efficient anode material for Li-ion batteries owing to its large surface area and complex morphology.

Acknowledgments

This work was supported by the National Research Foundation of Korea (NRF) grant funded by the Korea government (MEST) (No. 2012R1A2A2A01047579). Kishore Sridharan dedicates this work to his esteemed teacher, Late Professor R. Kalyanasundaram, Department of Chemistry, Government Arts College, Coimbatore and visiting faculty of the Department of Nanotechnology, Anna University Coimbatore for his inspiration.

Appendix A. Supplementary data

Supplementary data associated with this article can be found, in the online version, at http://dx.doi.org/10.1016/j.apcatb.2013.01.017.

References

[1] L. Cao, J.S. White, J.-S. Park, J.A. Schuller, B.M. Clemens, M.L. Brongersma, Nature Materials 8 (2009) 643–647.
[2] T. Trindade, P. O'Brien, N.L. Pickett, Chemistry of Materials 13 (2001) 3843–3858.
[3] J. Stangl, V. Holy, G. Bauer, Reviews of Modern Physics 76 (2004) 725–783.
[4] X. Fang, Y. Bando, U.K. Gautam, C. Ye, D. Golberg, Journal of Materials Chemistry 18 (2008) 509–522.
[5] K. Sridharan, V. Tamilselvan, D. Yuvaraj, K.N. Rao, R. Philip, Optical Materials 34 (2012) 639–645.
[6] V. Tamilselvan, K. Sridharan, K.N. Rao, R. Philip, Journal of Physics D: Applied Physics 43 (2010) 385402.
[7] G. Shen, P.C. Chen, K. Ryu, C. Zhou, Journal of Materials Chemistry 19 (2009) 828–839.
[8] X. Chen, S.S. Mao, Chemical Reviews 105 (2007) 2891–2959.
[9] Z. Sun, J.H. Kim, Y. Zhao, F. Bijarbooneh, V. Malgras, Y. Lee, Y.M. Kang, S.X. Dou, Journal of the American Chemical Society 133 (2011) 19314–19317.
[10] G. Liu, L.Z. Wang, H.G. Yang, H.M. Cheng, G.Q. Liu, Journal of Materials Chemistry 20 (2010) 831–843.
[11] K. Shankar, J.I. Basham, N.K. Allam, O.K. Varghese, G.K. Mor, X. Feng, M. Paulose, J.A. Seabold, K. Choi, C.A. Grimes, Journal of Physical Chemistry C 113 (2009) 6327–6359.
[12] X. Li, Y. Xiong, Z. Li, Y. Xie, Inorganic Chemistry 45 (2006) 3493–3495.
[13] Y. Wang, L. Zhang, K. Deng, X. Chen, Z. Zou, Journal of Physical Chemistry C 111 (2007) 2709–2714.
[14] M. Liu, L. Piao, W. Lu, S. Ju, L. Zhao, C. Zhou, H. Li, W. Wang, Nanoscale 2 (2010) 1115–1117.

[15] Y. Shengyuan, Z. Peining, A.S. Nair, S. Ramakrishana, Journal of Materials Chemistry 21 (2011) 6541–6548.
[16] X. Meng, D.W. Shin, S.M. Yu, J.H. Kim, H.M. Lee, Y.H. Han, V. Bhoraskar, J.B. Yoo, CrystEngComm 13 (2011) 3021–3029.
[17] M. Ge, J.W. Li, L. Liu, Z. Zhou, Industrial and Engineering Chemistry Research 50 (2011) 6681–6687.
[18] H. Zhou, Y. Qu, T. Zeid, X. Duan, Energy and Environmental Science 5 (2012) 6732–6743.
[19] M. Pelaez, N.T. Nolan, S.C. Pillai, M.K. Seery, P. Falaras, A.G. Kontos, P.S.M. Dunlop, J.W.J. Hamilton, J.A. Byrne, K. O'Shea, M.H. Entezari, D.D. Dionysiou, Applied Catalysis B: Environmental 125 (2012) 331–349.
[20] Y. Cao, T. He, Y. Chen, Y. Cao, Journal of Physical Chemistry C 114 (2010) 3627–3633.
[21] X. Li, R. Xiong, G. Wei, Journal of Hazardous Materials 164 (2009) 587–591.
[22] F. Fresno, D. Tudela, A.J. Maria, F. Rivera, J.M. Coronado, J. Soria, Applied Organometallic Chemistry 20 (2006) 220–225.
[23] H. Sayilkan, Applied Catalysis A: General 319 (2007) 230–236.
[24] E. Arpac, F. Sayilkan, M. Asilturk, P. Tatar, N. Kiraz, H. Sayilkan, Journal of Hazardous Materials 140 (2007) 69–74.
[25] F. Sayilkan, M. Asilturk, P. Tatar, N. Kiraz, S. Sener, E. Arpac, H. Sayilkan, Materials Research Bulletin 43 (2008) 127–134.
[26] V.B.R. Boppana, R.F. Lobo, Journal of Catalysis 281 (2011) 156–168.
[27] Y. Hosogi, Y. Shimodaira, H. Kato, H. Kobayashi, A. Kudo, Chemistry of Materials 20 (2008) 1299–1307.
[28] Y. Hosogi, H. Kato, A. Kudo, Journal of Physical Chemistry C 112 (2008) 17678–17682.
[29] S. Uma, J. Singh, V. Thakral, Inorganic Chemistry 48 (2009) 11624–11630.
[30] Q. Li, T. Kako, J. Ye, International Journal of Hydrogen Energy 36 (2011) 4716–4723.
[31] Y. Su, B. Zhu, K. Guan, S. Gao, L. Lv, C. Du, L. Peng, L. Hou, X. Wang, Journal of Physical Chemistry C 116 (2012) 18508–18517.
[32] J. Liu, Y. Zhao, L. Shi, S. Yuan, J. Fang, Z. Wang, M. Zhang, ACS Applied Materials and Interfaces 3 (2011) 1261-1268.
[33] B. Liu, E.S. Aydil, Journal of the American Chemical Society 131 (2009) 3985–3990.
[34] S.S. Mali, C.A. Betty, P.N. Bhosale, R.S. Devan, Y.R. Ma, S.S. Kolekar, P.S. Patil, CrystEngComm 14 (2012) 1920–1924.
[35] K. Mallick, S. Jewrajka, N. Pradhan, T. Pal, Current Science 80 (2001) 1408–1412.
[36] D. Wang, Y.N. Kumada, N. Kinomura, Chemistry of Materials 11 (1999) 2008–2012.
[37] J. Yang, C. Li, Z. Quan, C. Zhang, P. Yang, Y. Li, C. Yu, J. Lin, Journal of Physical Chemistry C 112 (2008) 12777–12785.
[38] Q. Zhang, J.B. Joo, Z. Lu, M. Dhal, D.Q.L. Olivera, M. Ye, Y. Yin, Nano Research 4 (2011) 103–114.
[39] C. Han, M. Pelaez, V. Likodimos, A.G. Kontos, P. Falaras, K. O'Shea, D.D. Dionysiou, Applied Catalysis B: Environmental 107 (2011) 77–87.
[40] P.S. Suchithra, C.P. Shadiya, A.P. Mohamed, P. Velusamy, S. Ananthakumar, Applied Catalysis B: Environmental 130–131 (2012) 44–53.
[41] J.R. Sambrano, G.F. Nóbrega, C.A. Taft, J. Andrés, A. Beltrán, Surface Science 580 (2005) 71–79.
[42] R. Long, Y. Dai, B. Huang, Journal of Physical Chemistry C 113 (2009) 650–653.
[43] P.A. Cox, R.G. Egdell, C. Harding, W.R. Patterson, P.J. Tavener, Surface Science 123 (1982) 179–203.
[44] M.H. Harunsani, F.E. Oropeza, R.G. Palgrave, R.G. Egdell, Chemistry of Materials 22 (2010) 1551–1558.
[45] D. Denzler, M. Olschewski, K. Sattler, Journal of Applied Physics 84 (1998) 2841.
[46] G.H. Olsen, C.J. Nuese, R.T. Smith, Journal of Applied Physics 49 (1978) 5523.
[47] A. Hagfeldt, M. Gratzel, Chemical Reviews 95 (1995) 49–68.
[48] I.S. Cho, D.W. Kim, S. Lee, C.H. Kwak, S.T. Bae, J.H. Noh, S.H. Yoon, H.S. Jung, D.W. Kim, K.S. Hong, Advanced Functional Materials 18 (2008) 2154–2162.
[49] H.G. Yang, C.H. Sun, S.Z. Qiao, J. Zou, G. Liu, S.C. Smith, H.M. Cheng, G.Q. Lu, Nature 453 (2008) 638.
[50] A.S. Barnard, Energy and Environmental Science 4 (2011) 439–443.
[51] T. Ohno, K. Sarukawa, M. Matsumura, New Journal of Chemistry 26 (2002) 1167.
[52] H.X. Li, Z.F. Bian, J. Zhu, D.Q. Zhang, G.S. Li, Y.N. Huo, H. Li, Y.F. Lu, Journal of the American Chemical Society 129 (2007) 8406–8407.
[53] G. Tian, Y. Chen, W. Zhou, K. Pan, C. Tian, X. Huang, H. Fu, CrystEngComm 13 (2011) 2994–3000.
[54] J.G. Yu, H.G. Yu, B. Cheng, X.J. Zhao, J.C. Yu, W.K. Ho, Journal of Physical Chemistry B 107 (2003) 13871–13879.
[55] I.K. Konstantinou, T.A. Albanis, Applied Catalysis B: Environmental 49 (2004) 1–14.
[56] M.R. Hoffmann, S.T. Martin, W. Choi, D.W. Bahnemann, Chemical Reviews 95 (1995) 69–96.
[57] A.L. Linsebigler, G. Lu, J.T. Yates, Chemical Reviews 95 (1995) 735–758.
[58] J. Yu, H. Yu, B. Cheng, M. Zhou, X. Zhao, Journal of Molecular Catalysis A 253 (2006) 112–118.
[59] T. Wu, G. Liu, J. Zhao, H. Hidaka, N. Serpone, Journal of Physical Chemistry B 102 (1998) 5845–5851.
[60] S. Rehman, R. Ullah, A.M. Butt, N.D. Gohar, Journal of Hazardous Materials 170 (2009) 560–569.
[61] X. Li, J. Ye, Journal of Physical Chemistry C 111 (2007) 13109–13116.
[62] K.I. Ishibashi, A. Fujishima, T. Watanabe, K. Hashimoto, Electrochemistry Communications 2 (2000) 207–210.
[63] J. Zhuang, W. Dai, Q. Tian, Z. Li, L. Xie, J. Wang, P. Liu, X. Shi, D. Wang, Langmuir 26 (2010) 9686–9694.